Nanoscale

PAPER

View Article Online
View Journal | View Issue

Cite this: *Nanoscale*, 2015, **7**, 18595

A CNT@$MoSe_2$ hybrid catalyst for efficient and stable hydrogen evolution†

Yunpeng Huang,[a] Hengyi Lu,[a] Huahao Gu,[a] Jun Fu,[b] Shuyi Mo,[b] Chun Wei,[b] Yue-E Miao*[c] and Tianxi Liu*[a,c]

Received 24th August 2015,
Accepted 5th October 2015

DOI: 10.1039/c5nr05739f

www.rsc.org/nanoscale

Exploration of high-efficiency Pt-free electrochemical catalysts for hydrogen evolution reaction (HER) is considered as a great challenge for the development of sustainable and carbon dioxide free energy conversion systems. In this work, a unique hierarchical nanostructure of few-layered $MoSe_2$ nanosheets perpendicularly grown on carbon nanotubes (CNTs) is synthesized through a one-step solvothermal reaction. This rationally designed architecture based on a highly conductive CNT substrate possesses fully exposed active edges and open structures for fast ion/electron transfer, thus leading to remarkable HER activity with a low onset potential of −0.07 V *vs.* RHE (reversible hydrogen electrode), a small Tafel slope of 58 mV per decade and excellent long-cycle stability. Therefore, this noble-metal-free and highly efficient catalyst enables prospective applications for industrial, renewable hydrogen production.

Introduction

Ever-increasing industrial growth and exhaustion of conventional fossil fuels call for innovation in energy conversion technology. Hydrogen, an important energy carrier, has been widely deployed as a promising fuel in future energy conversion systems to replace fossil fuels due to its high energy density and environmental friendliness.[1,2] Water splitting, which mainly relies on the catalytic activity of hydrogen evolution reaction (HER) catalysts, has been proved to be the most efficient and eco-friendly hydrogen production technique.[3,4] Platinum (Pt) and its alloys are undoubtedly the best HER catalysts in acidic medium due to their incomparable catalytic activity. However, the rarity and high cost severely limit their wide applications.[5,6] Hence, development of high-performance Pt-free HER catalysts based on earth-abundant materials is of great significance.[7–9]

Layered transition metal dichalcogenides (LTMDs), whose crystal structures are composed of covalently bonded X–M–X (M = Mo, W, *etc.*; X = S, Se, Te) layers by van der Waals forces like graphite,[10,11] have received much attention in energy conversion and storage fields due to their tunable band structure and intrinsic electrochemical properties.[12–17] MoS_2 and WS_2 based materials have been reported as high-performance HER catalysts and lithium-ion battery anodes in terms of remarkable catalytic activity and high capacity.[18–22] Recently, few-layer or monolayer $MoSe_2$ has emerged as a highly active electrocatalyst,[23] which has shown great potential in the electrochemical hydrogen production field due to its higher electrical conductivity and narrower bandgap than MoS_2.[24–30] Previous studies confirm that the unsaturated Se-edges in $MoSe_2$ nanosheets are extremely active as S-edges in MoS_2, which is responsible for the high HER activity.[25,29] Theoretical calculations also reveal that the Gibbs free energy for H_2 adsorption on $MoSe_2$ edges is lower than that of MoS_2, resulting in higher coverage of hydrogen adsorption.[26] Cui and coworkers reported a series of studies on few-layer $MoSe_2$ grown on various substrates including Si nanowires and Si wafer *via* high-temperature selenization, forming $MoSe_2$ thin films with vertically aligned layers and exposed edges to achieve excellent HER catalytic activity.[25,29] Wang *et al.*[31] prepared $MoSe_2$ on a novel reduced graphene oxide (rGO)/polyimide (PI) composite substrate by electrochemical deposition, which showed superior catalytic activity in both electrochemical and photoelectrical HER processes with a high cathode current at a more positive potential, excellent reversibility and stability. The small size of $MoSe_2$ nanoparticles and a highly conductive rGO/PI substrate were claimed to be responsible for the high catalytic activity. Hence, the rational design of high-performance $MoSe_2$ based HER catalysts should be based on two principles: (1) maximizing the density of electrochemically active sites or exposed edges of

[a]*State Key Laboratory of Molecular Engineering of Polymers, Department of Macromolecular Science, Fudan University, Shanghai, 200433, P. R. China*
[b]*Key Laboratory of New Processing Technology for Nonferrous Metals and Materials, Ministry of Education, Guilin University of Technology, Guilin, 541004, China*
[c]*State Key Laboratory for Modification of Chemical Fibers and Polymer Materials, College of Materials Science and Engineering, Donghua University, Shanghai 201620, China. E-mail: txliu@fudan.edu.cn, 12110440023@fudan.edu.cn; Fax: +86-21-65640293; Tel: +86-21-55664197*

†Electronic supplementary information (ESI) available: the FESEM image of CNT@$MoSe_2$-6 hybrid at low magnification; EDS mapping of CNT@$MoSe_2$-6 hybrid. See DOI: 10.1039/c5nr05739f

$MoSe_2$; (2) improving the electrical contact to these active sites by decreasing the number of $MoSe_2$ layers and hybridizing with other materials with good electrical conductivity.

Due to the intrinsic electrochemical activity and high surface area, carbon nanotubes (CNTs) are always employed as backbones in the development of advanced materials for energy and catalytic applications.[32–34] In this study, a novel CNT@$MoSe_2$ hybrid nanostructure was designed and fabricated through a facile one-step solvothermal reaction under low temperature. Encouragingly, this unique hybrid with perpendicularly oriented few-layered $MoSe_2$ nanosheets uniformly grown on CNTs exhibits excellent catalytic activity for HER with an extremely low onset potential and a small Tafel slope. On the one hand, one dimensional CNTs can direct the uniform distribution of few-layered $MoSe_2$ nanosheets, which effectively prevents the agglomeration and restacking of $MoSe_2$ nanosheets and maximizes the number of exposed active sites for fast ion/electrolyte transport. On the other hand, the backbone of CNTs with excellent electrical conductivity can ensure good electrical contact between perpendicularly oriented $MoSe_2$ nanosheets, thus greatly promoting electron transfer efficiency at the electrode interface.

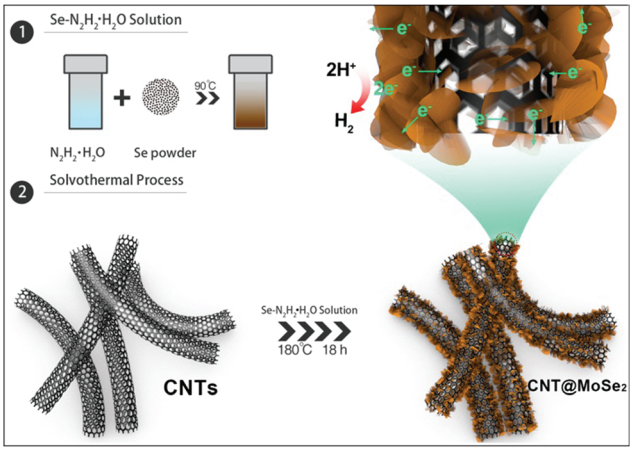

Scheme 1 Schematic illustration for the preparation of CNT@$MoSe_2$ hybrid.

Experimental

Materials

Multi-walled carbon nanotubes produced by the chemical vapor deposition method with an outer diameter of about 50 nm were supplied by Chengdu Institute of Organic Chemistry, Chinese Academy of Sciences, China. Selenium powder (Se, 99.99%), Na_2MoO_4 (99.99%), and hydrazine hydrate ($N_2H_4{\cdot}H_2O$, 50 wt% in water) were provided by Sinopharm Chemical Reagent Co. Ltd. The Pt/C catalyst (20 wt% platinum on carbon black) was purchased from Alfa Aesar. *N*,*N*-Dimethylformamide (DMF) and ethanol were obtained from Shanghai Chemical Reagent Company. All aqueous solutions were prepared with doubly distilled water.

Synthesis of CNT@$MoSe_2$ hybrids

The preparation procedure of CNT@$MoSe_2$ hybrids is schematically described in Scheme 1. First of all, pristine CNTs were treated with a mixture of H_2SO_4 and HNO_3 (1 : 1 v/v) at 90 °C for 1 h. After cooling to room temperature, the suspension was washed by filtration and dried in a vacuum oven at 50 °C for 24 h. The as-obtained acid-treated CNTs (20 mg) were dispersed in DMF (10 mL) by ultrasonication for 60 min. Meanwhile, a 4 mg mL^{-1} Se solution was prepared in a flask by adding a certain amount of Se powder into $N_2H_4{\cdot}H_2O$ solution. The greyish Se powder was soon dissolved in $N_2H_4{\cdot}H_2O$ to form a homogeneous dark-red solution after 1 h of magnetic stirring under a 80 °C oil bath. Afterwards, 10 mL of the Se solution was slowly dropped into the CNT suspension, with a stoichiometric amount of Na_2MoO_4 subsequently added into the above dispersion at a final Mo : Se molar ratio of 1 : 2. The mixture was transferred to a 40 mL Teflon-lined autoclave and heated at 180 °C for 12 h. After naturally cooling, the products were separated by high-speed centrifugation and washed with deionized water several times. After drying overnight, the black powder was annealed in N_2 at 450 °C with a ramp rate of 5 C min^{-1} for 2 h to finally yield a crystalized CNT@$MoSe_2$ hybrid. In order to optimize the loading amount of $MoSe_2$, different concentrations (2 mg mL^{-1}, 4 mg mL^{-1} and 6 mg mL^{-1}) of Se solutions were prepared for solvothermal reactions, with the corresponding products denoted as CNT@$MoSe_2$-2, CNT@$MoSe_2$-4 and CNT@$MoSe_2$-6, respectively. Pure $MoSe_2$ was also produced *via* the above method without the addition of CNTs.

Characterization

Morphology of the samples was observed using a field emission scanning electron microscope (FESEM, Zeiss) at an acceleration voltage of 5 kV. Transmission electron microscopy (TEM) was performed under an acceleration voltage of 200 kV with a Tecnai G2 20 TWIN TEM. Thermogravimetric analysis (Pyris 1 TGA) was performed under air flow from 100 to 700 °C at a heating rate of 20 °C min^{-1}. X-ray diffraction (XRD) experiments were conducted from 2θ = 10° to 80° on an X'Pert Pro X-ray diffractometer with Cu Kα radiation (λ = 0.1542 nm) under a voltage of 40 kV and a current of 40 mA. X-ray photoelectron spectroscopy (XPS) analyses were performed with a Thermo Scientific ESCALAB 250Xi using an Al Ka source 1846.6 eV anode. All XPS spectra were corrected using a C 1s line at 285 eV. Curve fitting and background subtraction were accomplished using XPS PEAK41 software.

Electrochemical measurements

Prior to all electrochemical measurements, a glassy carbon electrode (GCE) was sequentially polished with 1.0, 0.3 and 0.05 μm alumina slurries, and then ultrasonicated in a mixed solution of deionized water and ethanol (weight ratio = 1 : 1) for 5 min. Afterwards, the electrode was left to dry under a N_2

stream. Then, 2 mg of the CNT@$MoSe_2$ hybrid was dispersed in 1 mL of water along with 20 μL Nafion (5 wt% in ethanol) by at least 15 min sonication to form a homogeneous emulsion. Finally, 10 μL of the above slurry was dropped onto GCE (3 mm in diameter) to obtain CNT@$MoSe_2$ modified GCE. Electrodes with different loading amounts of the catalyst were obtained by repeatedly adding 5 μL of CNT@$MoSe_2$ slurry until reaching the required value. For comparison, bare CNTs, pure $MoSe_2$ and the commercially available Pt/C modified electrodes were also prepared in the same way.

All electrochemical HER tests were performed in a standard three-electrode setup using a CHI 660D electrochemical workstation (Shanghai Chenhua Instrument Co., China), where a platinum wire was used as the counter electrode, a saturated calomel electrode (SCE) as the reference electrode and the modified GCE as the working electrode. The final potential was calibrated to the reversible hydrogen electrode (RHE) by adding a value of (0.241 + 0.059 × pH) V for all the electrochemical tests. The electrocatalytic activity of the CNT@$MoSe_2$ hybrid catalyst towards HER was examined using linear sweep voltammetry (LSV) in nitrogen purged 0.5 M H_2SO_4 with a scan rate of 2 mV s^{-1} at room temperature. AC impedance measurements were carried out in 0.5 M H_2SO_4 from 10^{-2} to 10^6 Hz with an AC amplitude of 5 mV. Cycling tests were performed by recording LSV curves before and after 3000 cycles of cyclic voltammetry (CV) sweeps from −0.4 V to 0.2 V (*vs.* RHE) at 100 mV s^{-1}. The onset potential was determined based on the starting point of the linear region in the Tafel plot and no IR compensation was applied for all the electrochemical measurements.

Results and discussion

Morphology and structure of CNT@$MoSe_2$ hybrids

Fig. 1A shows the morphology of acid-treated CNTs with a smooth surface which interconnect with each other to form an integrated conducting network. After the solvothermal process involving Na_2MoO_4 as the Mo source and Se powder as the Se source, curled $MoSe_2$ nanosheets can be clearly observed on the outer surface of CNTs (Fig. 1B–F). At a lower Se concentration (Fig. 1B), only a few inconspicuous little flakes are scattered on CNTs, indicating the preliminary stage of reaction. For the CNT@$MoSe_2$-4 hybrid, well-defined $MoSe_2$ nanosheets are sparsely distributed along the CNT surface with an increased lateral length (Fig. 1C). It is also noticeable that the diameter of the CNT@$MoSe_2$-4 hybrid becomes larger with increasing Se dosage, implying that the growth of $MoSe_2$ is simultaneously along the lateral direction of the individual sheet. Further increasing the Se concentration to 6 mg mL^{-1}, perpendicularly oriented $MoSe_2$ nanosheets are evenly coated on CNTs with a denser distribution for the CNT@$MoSe_2$-6 hybrid, which is free from agglomeration and stacking (Fig. 1D and S1†). It is notable that even at a high loading amount of $MoSe_2$, the open spaces still can be retained in the CNT@$MoSe_2$-6 hybrid with perpendicularly oriented

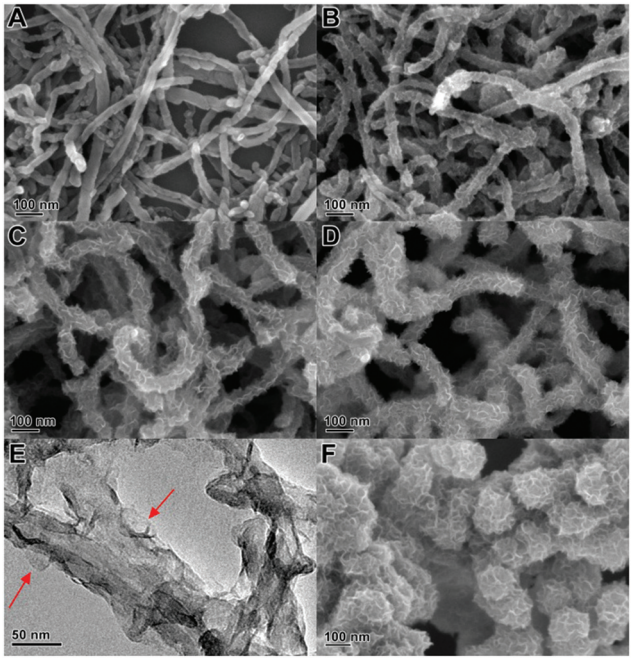

Fig. 1 FESEM images of (A) acid-treated CNTs, (B) CNT@$MoSe_2$-2, (C) CNT@$MoSe_2$-4, (D) CNT@$MoSe_2$-6 hybrids, (E) TEM image of CNT@$MoSe_2$-6 hybrid and (F) pure $MoSe_2$.

nanosheets, which are beneficial for ion diffusion and efficiently decrease the ion/electron transfer resistance. A zoom-in observation in Fig. 1E clearly reveals the distinct sheet-like morphology of $MoSe_2$ (indicated by red arrows). Energy dispersive X-ray spectroscopy (EDS) (Fig. S2†) confirms the existence of C, Mo and Se with the atomic ratio of Mo and Se being 1 : 1.9 (Si signal is ascribed to the sample substrate of silicon wafer), which is very close to the theoretical value of $MoSe_2$. It should be noted that the attempt to further increase the Se concentration is not feasible because it almost reaches the equilibrium concentration at 6 mg mL^{-1} for Se in $N_2H_4{\cdot}H_2O$. Nevertheless, pure $MoSe_2$ produced in the absence of the CNT substrate shows aggregated structures with wrinkled spherical configurations (Fig. 1F), which further manifests that the CNTs can serve as a good substrate to mediate the uniform growth of $MoSe_2$ nanosheets. Thus, the resulting hierarchical hybrid structure can provide numerous exposed active edges and shortened pathways for ion and electron transfer, which will potentially lead to enhanced electrochemical activity. Close observation by high-resolution TEM indicates that $MoSe_2$ in the hybrids is in the form of multiple $MoSe_2$ single layers with the interlayer spacing of 0.65 nm, in good accordance with the (002) lattice spacing of $MoSe_2$ (Fig. 2). $MoSe_2$ lattices are marked by red arrows while the CNT walls (*i.e.*, the substrate for the growth of $MoSe_2$ sheets) with the interlayer spacing of 0.34 nm are marked by white arrows. It is noticeable that the layered $MoSe_2$ nanosheet is composed of about 8–10 single layers, which can further increase the density of the exposed active edges and greatly improve the electrical contact

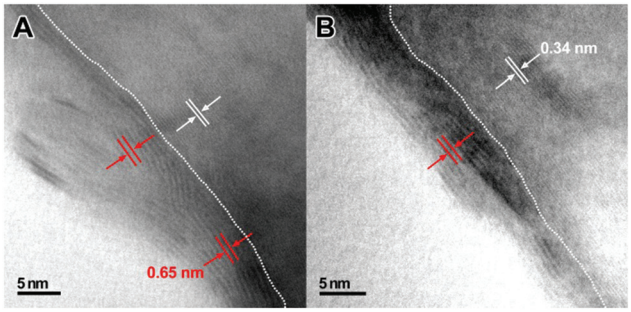

Fig. 2 (A, B) High-resolution TEM images of CNT@$MoSe_2$-6 hybrid.

between these active sites, thus potentially resulting in largely enhanced electrocatalytic HER activity.

Crystal structures of the as-synthesized CNT@$MoSe_2$-6 hybrid and pure $MoSe_2$ were studied using XRD as shown in Fig. 3. The sharp peak at 2θ = 26.1° in curve A can be readily indexed to the (002) diffraction plane of CNTs. As for pure $MoSe_2$ (Fig. 3B), the diffraction peaks at 2θ = 13.7°, 26.4°, 32.2°, 37.3°, 53.8°, 56.4°, 60.9° and 67.0° can be respectively indexed to the (002), (004), (100), (103), (106), (008), (107) and (202) diffraction planes of the hexagonal 2H-$MoSe_2$ phase (JCPDF card no. 87-2419), revealing the high purity of $MoSe_2$. In the XRD pattern of the CNT@$MoSe_2$-6 hybrid (Fig. 3C), diffraction peaks of (002), (100), (103), (106) and (008) can be clearly observed although the (004) peak of $MoSe_2$ is overlapped with the (002) diffraction plane of CNTs, indicating the successful growth of $MoSe_2$ on the CNT template. In order to further analyze the chemical composition and valence states of the CNT@$MoSe_2$-6 hybrid, XPS analysis was conducted (Fig. 4). The survey spectrum in Fig. 4A indicates the presence of Mo, Se, O, and C elements in the hybrids, which is in good

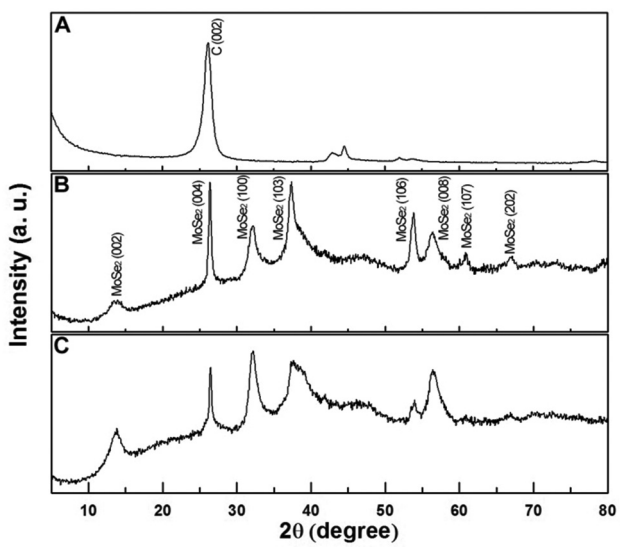

Fig. 3 XRD patterns of (A) bare CNTs, (B) pure $MoSe_2$ nanospheres, and (C) CNT@$MoSe_2$-6 hybrid.

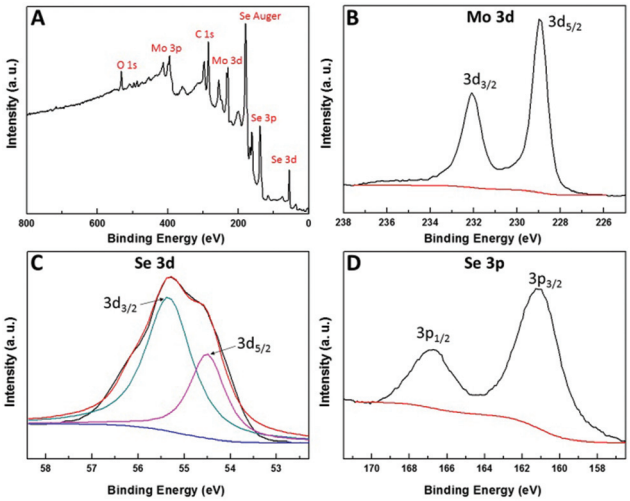

Fig. 4 XPS spectra of CNT@$MoSe_2$-6 hybrid: (A) survey spectrum, (B) Mo 3d, (C) Se 3d and (D) Se 3p.

agreement with the EDS results (Fig. 1E). The high-resolution spectrum of Mo 3d exhibits two peaks at 228.9 and 232.1 eV assigned to Mo $3d_{5/2}$ and Mo $3d_{3/2}$ orbitals, respectively, confirming the formation of Mo^{4+}. Meanwhile, the Se 3d can be deconvoluted into Se $3d_{5/2}$ and Se $3d_{3/2}$ at 54.5 and 55.2 eV, respectively, along with Se $3p_{3/2}$ and Se $3p_{1/2}$ at 160.8 and 166.6 eV, all indicating the oxidation state of Se^{2-}. Moreover, the detailed compositional analysis reveals that the surface atomic ratio of Mo : Se is 10 : 21, which is close to the formula of $MoSe_2$.

TGA measurements were conducted to further determine the loading percentage of $MoSe_2$ in the hybrids. As shown in Fig. 5, the acid-treated CNTs are burnt out in air at 700 °C, while pure $MoSe_2$ undergoes 10% weight increment between 200 °C and 315 °C, which is in accordance with the work

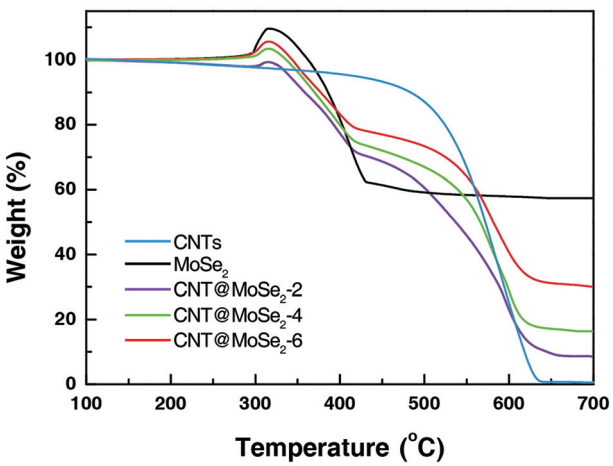

Fig. 5 TGA curves for bare CNTs, pure $MoSe_2$ nanospheres and CNT@$MoSe_2$ hybrids.

reported previously,[35] and can be explained as follows. At a low temperature of 200 °C, $MoSe_2$ starts to pyrolyze as $2MoSe_2 + 7O_2 = 2MoO_3 + 4SeO_2$, resulting in solid-state SeO_2 with a total weight increment. As the temperature reaches the sublimation temperature of SeO_2, *i.e.*, 315 °C, SeO_2 starts to volatilize with the total weight decreasing to 57.3% of the initial weight, which results in the final residue of MoO_3. For the case of CNT@$MoSe_2$ hybrids, TGA curves exhibit a two-stage weight loss process, where SeO_2 gasifies at the first stage and CNTs convert into CO_2 at the second stage. Based on the TGA curves, the loading percentages of $MoSe_2$ in CNT@$MoSe_2$-2, CNT@$MoSe_2$-4, and CNT@$MoSe_2$-6 hybrids are calculated to be about 14.4%, 28.9% and 53.2%, respectively. This pretty high loading amount is probably due to the high surface area of the CNTs, which provides substantial nucleation sites for the growth of $MoSe_2$ nanosheets.

Electrochemical evaluation of the HER catalyst

The electrocatalytic HER activity of all the materials deposited on GCE was investigated in 0.5 M H_2SO_4 solution by employing a typical three-electrode setup. In general, an ideal HER catalyst is a material that can provide a high current at low overpotentials, along with a low HER onset potential (*i.e.*, the potential at which the hydrogen evolution reaction begins) comparable to that of a Pt based catalyst. To start with, electrochemical activities of CNT@$MoSe_2$ hybrids with different loading percentages were measured for a preliminary comparison (Fig. 6). LSV curves of CNT@$MoSe_2$-2 and CNT@$MoSe_2$-4 modified GCE show almost the same onset potential of about −0.12 V *vs.* RHE, though the CNT@$MoSe_2$-4 hybrid exhibits an enhanced HER current density compared with the CNT@$MoSe_2$-2 one. However, the curve of the CNT@$MoSe_2$-6 hybrid is much more positively shifted with a lower onset potential of −0.07 V *vs.* RHE which outperforms most of the previously reported MoS_2- or $MoSe_2$-based HER catalysts (detailed comparisons are provided in Table 1). Moreover, the CNT@$MoSe_2$-6 hybrid exhibits a current density of 10 mA cm^{-2} at a lower overpotential of 0.178 V which is much smaller than that of CNT@$MoSe_2$-2 (10 mA cm^{-2} at 0.212 V) and CNT@$MoSe_2$-4 (10 mA cm^{-2} at 0.202 V). Possible reasons for the different HER electrocatalytic activities can be deduced from the morphological difference as observed from Fig. 1B–D. The CNT@$MoSe_2$-6 hybrid shows an optimized hierarchical structure with more uniform distribution of $MoSe_2$ nanosheets and exposed active edges compared with CNT@$MoSe_2$-2 and CNT@$MoSe_2$-4 hybrids, which may provide a large contact area for the HER process and greatly facilitate fast ion/electron transfer, thus leading to the highest HER catalytic activity.

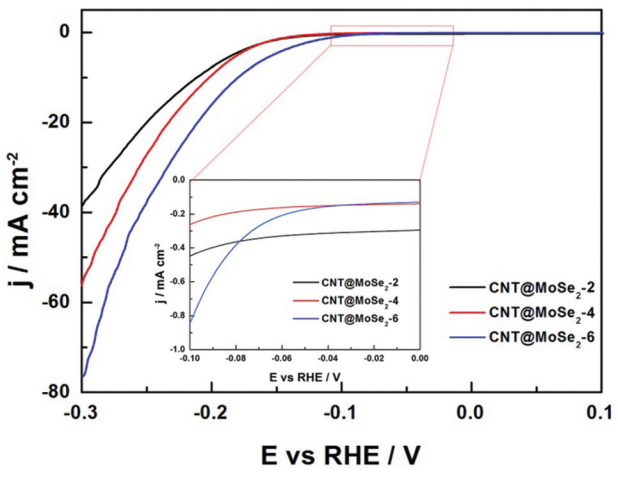

Fig. 6 LSV polarization curves for CNT@$MoSe_2$-2, CNT@$MoSe_2$-4 and CNT@$MoSe_2$-6 hybrid modified GCE in N_2-purged 0.5 M H_2SO_4 solution. Scan rate: 2 mV s^{-1} (inset: magnified region close to the onset potentials).

Further comparisons of HER activity between bare CNT, pure $MoSe_2$, CNT@$MoSe_2$-6 hybrids and commercially available Pt/C catalysts were also performed. As shown in Fig. 7A, the Pt/C catalyst exhibits extremely high HER catalytic activity with a near zero onset potential and large current density at the same overpotential. Contrarily, bare CNT modified GCE shows almost no HER activity with a near flat line within the potential window. The pure $MoSe_2$ exhibits distinctive HER activity owing to the intrinsic electrocatalytic activity of LTMD, but with much lower anodic current and more negative onset potential (−0.16 V) compared with those of the CNT@$MoSe_2$-6 hybrid. This may be attributed to the severe aggregation of pure $MoSe_2$ spheres with limited exposed edges and insufficient active sites. Therefore, the excellent HER catalytic activity of the CNT@$MoSe_2$-6 hybrid indicates the successful design of this unique hierarchical architecture, which incorporates the merits of both components in a reasonable manner to achieve synergistically enhanced HER performance. Fig. 7B presents the Tafel plots of different electrodes derived from their corresponding LSV curves, which usually represent the inherent electrocatalytic properties determined by the rate limiting steps of HER. The Tafel slope, which can be deduced from the Tafel equation ($\eta = b\log(j) + a$, where η is the overpotential, j is the current density and b is the Tafel slope), is correlated with the reaction pathway and adsorption type. Tafel slopes for Pt/C, pure $MoSe_2$, and CNT@$MoSe_2$-6 hybrids are about 34, 74 and 58 mV per decade, respectively. The smaller Tafel slope of the CNT@$MoSe_2$-6 hybrid than that of pure $MoSe_2$ means a faster increase of the HER rate with the increment of overpotential, which is attractive for practical applications. Additionally, with a Tafel slope of 58 mV per decade, the HER process of the CNT@$MoSe_2$-6 catalyst can be assigned as the Volmer–Heyrovsky or the Volmer–Tafel mechanism with the Volmer reaction as the rate-determine step.[22]

The dependence of HER activity on different loading amounts of the CNT@$MoSe_2$-6 catalyst on GCE is shown in Fig. 8. From the LSV curves in Fig. 8A, we can conclude that the optimal loading amount is 15 μL (2 mg mL^{-1}) with large current densities of 4.6 and 16.1 mA cm^{-2} at overpotentials of 150 and 200 mA, respectively (Fig. 8B). Generally, the HER catalytic performance directly rests on the amount of active

Table 1 Comparison on the HER performance between different materials

Catalyst	Synthesis method	Electrolyte	Onset potential (V *vs.* RHE)	Overpotential (V *vs.* RHE) at 10 mA cm^{-2}	Tafel slope (mV per decade)	Ref.
CNT@$MoSe_2$	Solvothermal	0.5 M H_2SO_4	−0.07	0.178	58	This work
S-doped $MoSe_2$	Reflux method	0.5 M H_2SO_4	−0.09	~0.10	60	30
$MoSe_{2-x}$ ($x \sim 0.47$)	Colloidal synthesis	0.5 M H_2SO_4	−0.17	~0.28	98	36
$MoSe_2$/graphene	CVD	0.5 M H_2SO_4	−0.05	0.159	61	27
$MoSe_2$	CVD	0.5 M H_2SO_4	−0.2	>0.4	105–120	29
$MoSe_2$	CVD	0.5 M H_2SO_4	−0.11	0.25	59.8	25
$MoSe_2$/rGO	Hydrothermal	0.5 M H_2SO_4	−0.05	0.15	69	26
MoS_2/SnO_2	Solvothermal	0.5 M H_2SO_4	−0.15	~0.22	59	22
Exfoliated MoS_2	Ultrasonication	0.5 M H_2SO_4	−0.12	~0.21	70	19
MoS_2	CVD	0.5 M H_2SO_4	−0.15	0.187	43	14

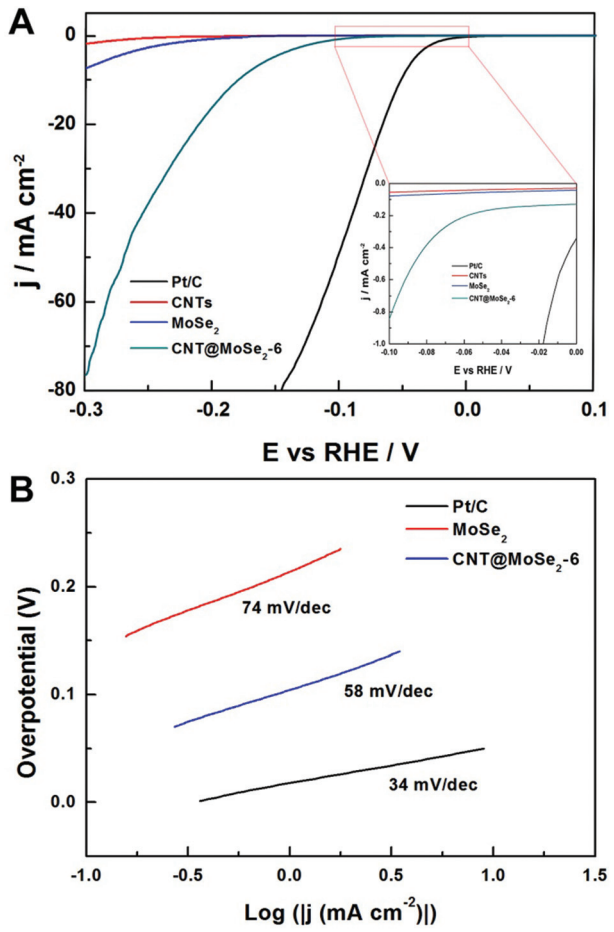

Fig. 7 (A) LSV polarization curves for GCE modified with different materials in N_2-purged 0.5 M H_2SO_4 solution. Scan rate: 2 mV s^{-1} (inset: magnified region close to the onset potentials). (B) Tafel plots for Pt/C, pure $MoSe_2$ and CNT@$MoSe_2$-6 hybrid modified GCE.

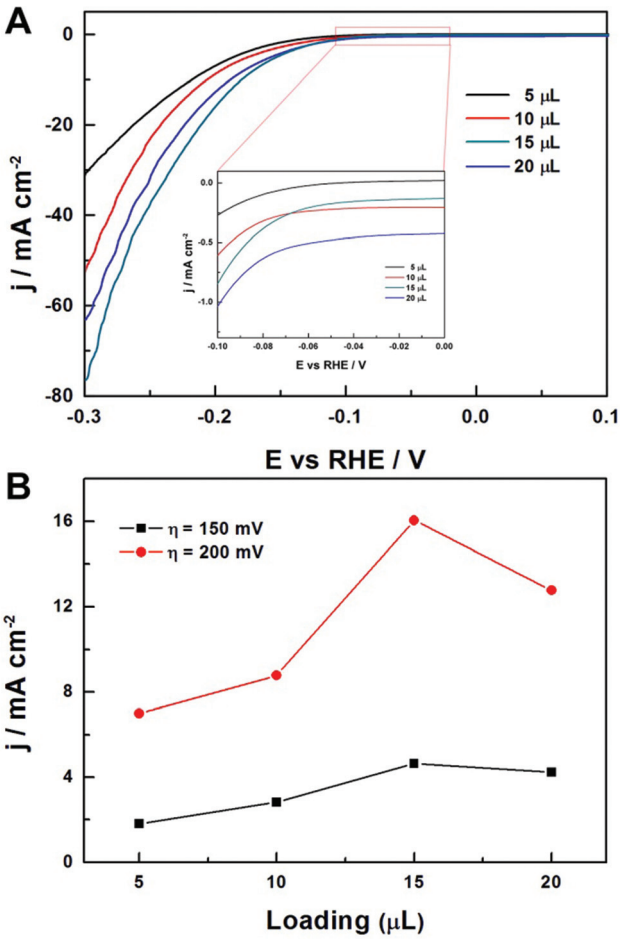

Fig. 8 (A) LSV polarization curves for CNT@$MoSe_2$-6 hybrid modified GCE with different loading amounts in N_2-purged 0.5 M H_2SO_4 solution. Scan rate: 2 mV s^{-1} (inset: magnified region close to the onset potentials). (B) The corresponding current densities at overpotentials of 150 mV and 200 mV.

sites offered by the catalyst. Therefore, the higher loading amount of the catalyst may provide more active sites. However, excessive loading of the CNT@$MoSe_2$-6 catalyst would cause restacking and aggregation of active edges, thus leading to inferior HER performance.

Long-cycle durability of the HER catalyst is of vital significance in practical applications. Hence, cyclic voltammetry (CV) of CNT@$MoSe_2$-6 modified GCE was conducted for 3000 cycles from −0.4 V to 0.2 V (*vs.* RHE) at 100 mV s^{-1}, with the LSV

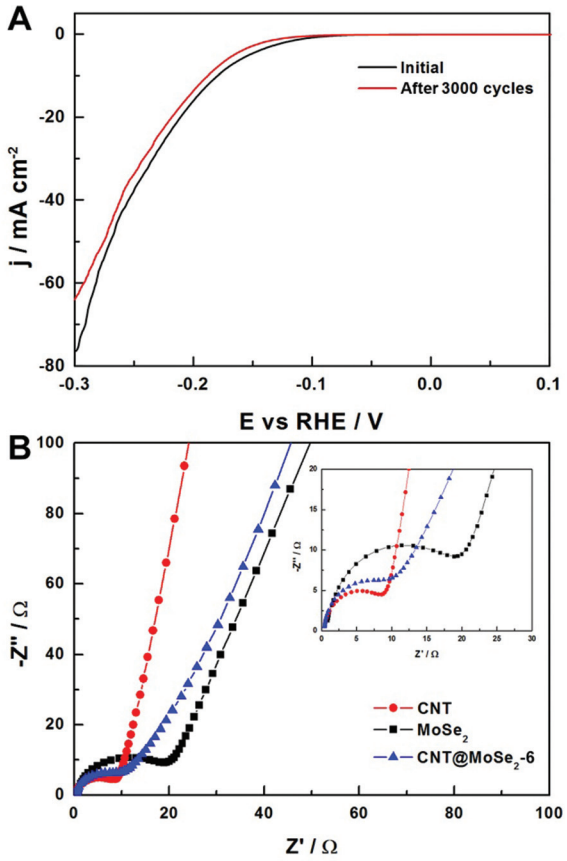

Fig. 9 (A) LSV polarization curves for CNT@$MoSe_2$-6 modified GCE recorded before and after 3000 cycles of CV scanning. (B) Nyquist plots for bare CNTs, pure $MoSe_2$, and CNT@$MoSe_2$-6 modified electrodes.

curves before and after CV tests shown in Fig. 9A. It can be seen that the catalyst retains the same low onset potential with a slight decay of the current density, indicating the good durability of the as-synthesized catalyst. EIS tests were further conducted for bare CNTs, pure $MoSe_2$ and CNT@$MoSe_2$-6 electrodes to investigate their electrochemical behavior during the HER process. As shown in Fig. 9B, the visible semicircles in a high frequency region are mainly due to the charge transfer resistance (R_{ct}) of H^+ reduction at the electrode–electrolyte interface. In addition, the series resistance (R_s) can be deduced from the *x*-intercept of Nyquist plots. Obviously, R_{ct} of the CNT@$MoSe_2$-6 electrode is lower than that of pure $MoSe_2$, indicating that the CNTs with a larger surface area can help the uniform distribution of few-layer $MoSe_2$ nanosheets, thus significantly decreasing the ion transfer resistance along the electrode–electrolyte interface. Furthermore, the smaller R_s of the CNT@$MoSe_2$-6 hybrid with respect to pure $MoSe_2$ nanospheres implies that the intimate coupling between perpendicularly oriented $MoSe_2$ and highly conductive CNTs can provide efficient pathways for fast electron transfer. These analytical pieces of evidence further highlight the rational design of this hierarchical CNT@$MoSe_2$ nanostructure for a high-performance noble-metal-free HER catalyst.

Conclusions

In summary, a one-step low-temperature solvothermal method has been demonstrated for the successful preparation of perpendicularly oriented few-layered $MoSe_2$ nanosheets on the CNT template. This rationally designed hierarchical architecture not only realizes the uniform distribution of $MoSe_2$ nanosheets by virtue of the high surface area of conductive CNTs, but also affords intimate coupling between these two components. The resulting open structure of $MoSe_2$ nanosheets with fully exposed active sites facilitates fast ion/electron transfer, leading to excellent HER catalytic performance with a low onset potential of −0.07 V *vs.* RHE and a small Tafel slope of 58 mV per decade. Therefore, this study opens a new avenue for the development of a high-performance Pt-free HER catalyst.

Acknowledgements

The authors are grateful for the financial support from the National Natural Science Foundation of China (51125011, 51373037, 51433001), the Guangxi Small Highland Innovation Team of Talents in Colleges and Universities, the Guangxi Funds for Specially-appointed Expert, and the Guangxi Natural Science Foundation of China (No. 2014GXNSFAA118321).

References

1 M. S. Dresselhaus and I. L. Thomas, *Nature*, 2001, **414**, 332–337.
2 J. A. Turner, *Science*, 2004, **305**, 972–974.
3 J. Greeley, T. F. Jaramillo, J. Bonde, I. Chorkendorff and J. K. Norskov, *Nat. Mater.*, 2006, **5**, 909–913.
4 D. J. Li, U. N. Maiti, J. Lim, D. S. Choi, W. J. Lee, Y. Oh, G. Y. Lee and S. O. Kim, *Nano Lett.*, 2014, **14**, 1228–1233.
5 J. R. McKone, E. L. Warren, M. J. Bierman, S. W. Boettcher, B. S. Brunschwig, N. S. Lewis and H. B. Gray, *Electrochim. Acta*, 2011, **4**, 3573–3583.
6 B. E. Conway and B. V. Tilak, *Electrochim. Acta*, 2002, **47**, 3571–3594.
7 P. Jiang, Q. Liu, Y. H. Liang, J. Q. Tian, A. M. Asiri and X. P. Sun, *Angew. Chem., Int. Ed.*, 2014, **53**, 12855–12859.
8 S. J. Peng, L. L. Li, X. P. Han, W. P. Sun, M. Srinivasan, S. G. Mhaisalkar, F. Y. Cheng, Q. Y. Yan, J. Chen and S. Ramakrishna, *Angew. Chem., Int. Ed.*, 2014, **53**, 12594–12599.
9 Y. Yang, H. L. Fei, G. D. Ruan, C. S. Xiang and J. M. Tour, *Adv. Mater.*, 2014, **26**, 8163–8168.
10 G. Eda, H. Yamaguchi, D. Voiry, T. Fujita, M. W. Chen and M. Chhowalla, *Nano Lett.*, 2011, **11**, 5111–5116.
11 L. Sun, Y. L. Ying, H. B. Huang, Z. G. Song, Y. Y. Mao, Z. P. Xu and X. S. Peng, *ACS Nano*, 2014, **8**, 6304–6311.

12 Q. H. Wang, K. Kalantar-Zadeh, A. Kis, J. N. Coleman and M. S. Strano, *Nat. Nanotechnol.*, 2012, **7**, 699–712.
13 J. Lin, Z. W. Peng, G. Wang, D. Zakhidov, E. Larios, M. J. Yacaman and J. M. Tour, *Adv. Energy Mater.*, 2014, **4**, 1301875.
14 M. A. Lukowski, A. S. Daniel, F. Meng, A. Forticaux, L. S. Li and S. Jin, *J. Am. Chem. Soc.*, 2013, **135**, 10274–10277.
15 J. K. Huang, J. Pu, C. L. Hsu, M. H. Chiu, Z. Y. Juang, Y. H. Chang, W. H. Chang, Y. Iwasa, T. Takenobu and L. J. Li, *ACS Nano*, 2013, **8**, 923–930.
16 C. M. Huang, S. F. Wu, A. M. Sanchez, J. J. P. Peters, R. Beanland, J. S. Ross, P. Rivera, W. Yao, D. H. Cobden and X. D. Xu, *Nat. Mater.*, 2014, **13**, 1096–1101.
17 L. Cheng, W. J. Huang, Q. F. Gong, C. H. Liu, Z. Liu, Y. G. Li and H. J. Dai, *Angew. Chem., Int. Ed.*, 2014, **53**, 7860–7863.
18 F. Zhou, S. Xin, H. W. Liang, L. T. Song and S. H. Yu, *Angew. Chem., Int. Ed.*, 2014, **53**, 11552–11556.
19 S. S. Ji, Z. Yang, C. Zhang, Z. Y. Liu, W. W. Tjiu, I. Y. Phang, Z. Zhang, J. S. Pan and T. X. Liu, *Electrochim. Acta*, 2013, **109**, 269–275.
20 S. J. Xu, D. Li and P. Y. Wu, *Adv. Funct. Mater.*, 2015, **25**, 1127–1136.
21 D. B. Kong, H. Y. He, Q. Song, B. Wang, W. Lv, Q. H. Yang and L. J. Zhi, *Energy Environ. Sci.*, 2014, **7**, 3320–3325.
22 Y. P. Huang, Y. E. Miao, L. S. Zhang, W. W. Tjiu, J. S. Pan and T. X. Liu, *Nanoscale*, 2014, **6**, 10673–10679.
23 Y. P. Huang, Y. E. Miao, J. Fu, S. Y. Mo, C. Wei and T. X. Liu, *J. Mater. Chem. A*, 2015, **3**, 16263–16271.
24 Y. F. Shi, C. X. Hua, B. Li, X. P. Fang, C. H. Yao, Y. C. Zhang, Y. S. Hu, Z. X. Wang, L. Q. Chen, D. Y. Zhao and G. D. Stucky, *Adv. Funct. Mater.*, 2013, **23**, 1832–1838.
25 H. T. Wang, D. S. Kong, P. Johanes, J. J. Cha, G. Y. Zheng, K. Yan, N. Liu and Y. Cui, *Nano Lett.*, 2013, **13**, 3426–3433.
26 H. Tang, K. P. Dou, C. C. Kaun, Q. Kuang and S. H. Yang, *J. Mater. Chem. A*, 2014, **2**, 360–364.
27 S. Mao, Z. H. Wen, S. Q. Ci, X. R. Guo, K. K. Ostrikov and J. H. Chen, *Small*, 2015, **11**, 414–419.
28 H. Wang, X. Y. Wang, L. Wang, J. Wang, D. L. Jiang, G. P. Li, Y. Zhang, H. H. Zhong and Y. Jiang, *J. Phys. Chem. C*, 2015, **119**, 10197–10205.
29 D. S. Kong, H. T. Wang, J. J. Cha, M. Pasta, K. J. Koski, J. Yao and Y. Cui, *Nano Lett.*, 2013, **13**, 1341–1347.
30 C. Xu, S. J. Peng, C. L. Tan, H. X. Ang, H. T. Tan, H. Zhang and Q. Y. Yan, *J. Mater. Chem. A*, 2014, **2**, 5597–5601.
31 L. P. Jia, X. Sun, Y. M. Jiang, S. J. Yu and C. M. Wang, *Adv. Funct. Mater.*, 2015, **25**, 1814–1820.
32 W. J. Lee, J. M. Lee, S. T. Kochuveedu, T. H. Han, H. Y. Jeong, M. Park, J. M. Yun, J. Kwon, K. No, D. H. Kim and S. O. Kim, *ACS Nano*, 2012, **6**, 935–943.
33 U. N. Maiti, W. J. Lee, J. M. Lee, Y. Oh, J. Y. Kim, J. E. Kim, J. Shim, T. H. Han and S. O. Kim, *Adv. Mater.*, 2014, **26**, 40–67.
34 W. J. Lee, U. N. Maiti, J. M. Lee, J. Lim, T. H. Han and S. O. Kim, *Chem. Commun.*, 2014, **50**, 6818–6830.
35 Y. Liu, M. Q. Zhu and D. Chen, *J. Mater. Chem. A*, 2015, **3**, 11857–11862.
36 X. L. Zhou, J. Jiang, T. Ding, J. J. Zhang, B. C. Pan, J. Zuo and Q. Yang, *Nanoscale*, 2014, **6**, 11046–11051.